A Simple Front-End for Pulse Oximeters With a Direct Light-to-Time-to-Digital Interface Circuit

José A. Hidalgo-López, *Member, IEEE*

***Abstract*—Pulse oximeters are electronic devices that provide the values of two physiological parameters: heart rate (HR) and functional O_2 saturation, SpO_2. Acquiring this information requires a photodiode and a set of red and infrared light-emitting diodes (LEDs) to generate two plethysmograms, which are digitally processed to find the HR and SpO_2 values. The circuits currently used to generate these plethysmograms require multiple analog modules, such as voltage references, transimpedance amplifiers (TIAs), voltage amplifiers, and comparators. Analog-to-digital converters (ADCs) or switched integrators (SIs) are also needed to digitalize the signals that provide the HR and SpO_2 values when introduced in a digital processor (DP). This article proposes a new circuit that eliminates the need for all these analog modules or converters, replacing them with a single capacitor and two resistors. The circuit is based on a light-to-time-to-digital conversion performed using the DP, which does not require any special characteristics to carry out this task. As a proof of concept, the new design has been implemented using a field-programmable gate array (FPGA) as the DP. The results show plethysmograms with good detail regarding amplitude and time, allowing the device to be used for clinical purposes. A comparison with two conventional commercial pulse oximeters shows that the new circuit provides similar HR and SpO_2 values.**

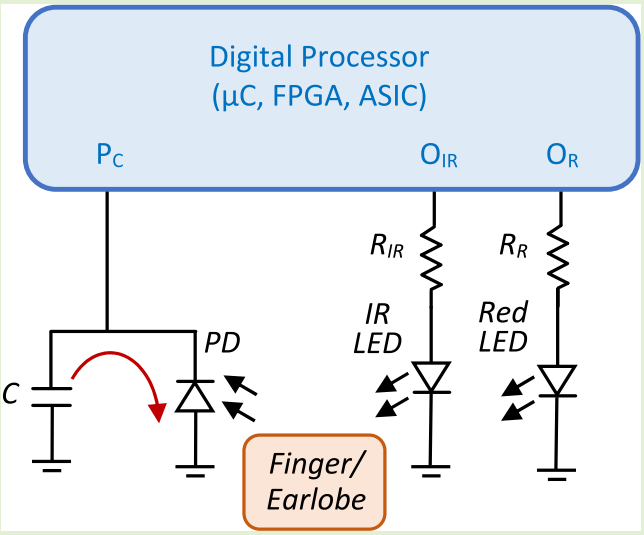

***Index Terms*— Direct interface circuit (DIC), light-to-time-to-digital, photoplethysmography, pulse oximetry.**

I. Introduction

PULSE waves include large quantities of physiological and pathological information, of which pulse rate and oxygen saturation provide the most details [1], [2], [3]. Monitoring these parameters gives information about heart and lung function, organ-specific perfusion, cardiovascular status, hypoxia diagnosis, and so on. The use of such data has progressively extended beyond the medical field into sports and subsequently to the public, who use wearable devices for real-time information on their health. Due to humans' inherent inquisitiveness regarding health-related topics, pulse oximeters [devices capable of offering data on, at the very least, heart rate (HR) and functional oxygen saturation (SpO_2)] have become a category of electronic tools that immediately attract attention. Mass use of these devices means efficient hardware and power consumption design is more important than ever.

Conventional pulse oximetry uses two light wavelengths [red and near-infrared (IR)] transmitted/reflected through the distal phalanx of the finger or the earlobe [4]. A photodetector senses these transmitted/reflected lights. Pulse oximeter functionality is based on hemoglobin (Hb) color changes from dark to bright red when oxygenated. Oxyhemoglobin (HbO_2) absorbs higher amounts of IR light and lower amounts of red light than Hb [5]. It is fortuitous that HbO_2 and Hb have significant differences in red and IR light absorption, as these two wavelengths effectively permeate tissues, unlike others that experience substantial absorption by nonvascular tissues and water [6]. This difference in light absorption properties between HbO_2 and Hb is exploited in conventional pulse oximeters using two small light-emitting diodes (LEDs): red at 660-nm and IR at 940-nm wavelengths. A broadband photodiode then detects the light transmitted/reflected through

Manuscript received 30 October 2023; accepted 6 November 2023. Date of publication 21 November 2023; date of current version 2 January 2024. This work was supported by the Spanish Government under Grant PID2021-125091OB-I00. Funding for open access charge: Universidad de Málaga / CBUA. The associate editor coordinating the review of this article and approving it for publication was Prof. Benoit Gosselin.

This work involved human subjects or animals in its research. The author confirms that all human/animal subject research procedures and protocols are exempt from review board approval.

The author is with the Departamento de Electrónica, Universidad de Málaga, 29071 Málaga, Spain (e-mail: jahidalgo@uma.es).

Digital Object Identifier 10.1109/JSEN.2023.3333055

© 2023 The Authors. This work is licensed under a Creative Commons Attribution 4.0 License.
For more information, see https://creativecommons.org/licenses/by/4.0/

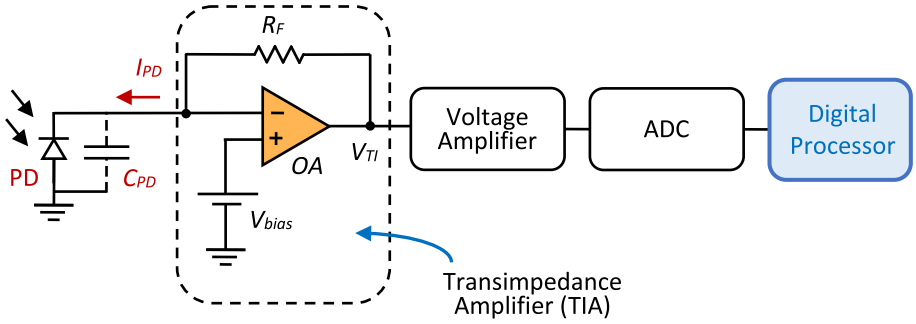

Fig. 1. Classic circuit for light-to-voltage-to-digital conversion in a pulse oximeter.

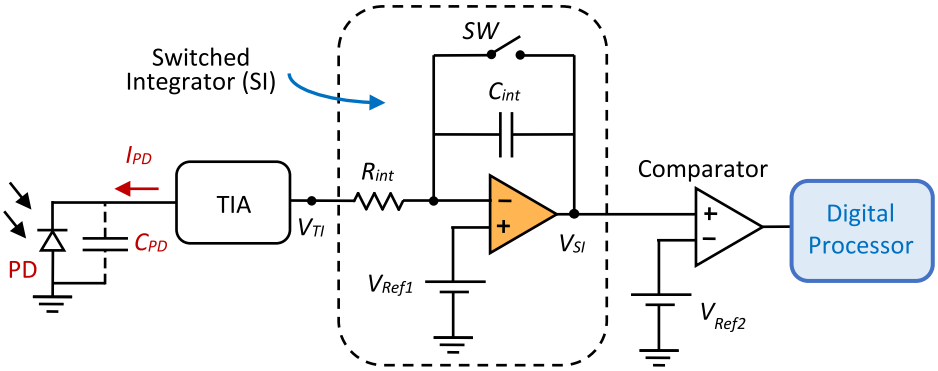

Fig. 2. Light-to-voltage-to-time-to-digital conversion scheme in a pulse oximeter.

the finger or earlobe. Variations in the amounts of red and IR light received at the photodiode determine the oxygen saturation ratio of Hb in arterial blood (SpO_2 value). The frequency in the change of the amount of IR light received is also often used as the HR value [1].

Conventional pulse oximeters first perform light-to-voltage-to-digital conversion, followed by digital signal processing that provides the HR and SpO_2 values [7]. There are systems of different degrees of complexity to perform this conversion. For example, in [8], a complex chopper network converts the photocurrent signal into a voltage. However, this is usually done using a transimpedance amplifier (TIA) [9], followed by a voltage amplifier that feeds the signal to an analog-to-digital converter (ADC) [10], [11], [12], [13], [14], [15], [16], [17]. A general layout for this kind of circuit is shown in Fig. 1. The TIA transforms the information provided by the photodiode into the form of a current into a voltage [18]. Fig. 1 also shows the output capacitance of the photodiode (C_{PD}), which may slightly distort the output value of the TIA. The amplifier's positive input is used to supply a reverse-bias voltage, V_{bias} in Fig. 1, for the photodiode, such that the current in this element, I_{PD}, is mainly due to the amount of light it receives. The design presented in [19] (also based on using a TIA followed by an ADC) is particularly worthy of note, as here, the LEDs are replaced by silicon nanowires, while several modifications are introduced in the circuit to reduce reading errors. The circuits are complex for all of these designs since, together with the ADC, several operational amplifiers (OAs) and discrete elements are needed for implementation.

A different approach is presented in [20], where a light-to-voltage-to-time-to-digital conversion is carried out (Fig. 2). In this circuit, a voltage mode switched integrator (SI) follows the TIA. The switch (SW) in Fig. 2 is closed when no LEDs are activated, such as $V_{SI} = V_{Ref1}$. When an LED is activated, SW opens, and V_{SI} increases linearly over time, with a constant of proportionality related to the current flowing through the photodiode. V_{SI} is fed into a comparator that generates a binary signal that takes a "1" value for a time inversely related to the value of I_{PD}. The same circuit layout is used in [21] with some minor changes [22], [23], [24] also use this architecture with different types of TIAs. Although circuits based on this type of architecture are simpler than those based on TIA-ADC, they are still complex circuits with OAs, switches, and additional reference voltage sources. An excellent review of the state of the art of photoplethysmographic sensors based on the structures shown in Figs. 1 and 2 can be found in [25].

All the aforementioned circuits require a digital processor (DP), which, based on the digital values of the output signal, provides HR and SpO_2. In these implementations, the DP merely receives the digital information without being actively involved in acquiring data.

However, direct interface circuits (DICs) [26], using DPs as part of an analog front-end, allows circuits to be simplified. DICs have been widely used in resistive, capacitive, and inductive sensor readout circuits [27], [28], [29], [30]. In DICs, the magnitude of the variable to be measured is established based on the discharge times of one or more capacitors that have previously been charged to a voltage set by one of the

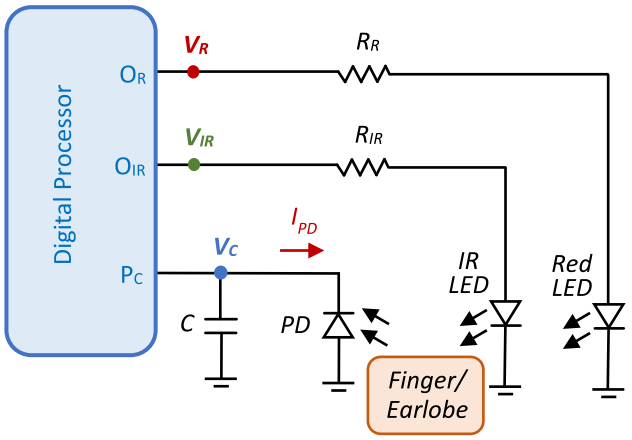

Fig. 3. New proposed circuit for a pulse oximeter.

DP's output pins, performing a magnitude-to-time-to-digital conversion.

Despite its simplicity, to the best of our knowledge, the ideas underlying DICs have never been used to design a front-end of a pulse oximeter. This article proposes a new front-end based on such DICs. The new architecture significantly reduces the hardware without any tradeoff with other device parameters. As proof of concept, a pulse oximeter has been implemented using a field-programmable gate array (FPGA) as the DP. The results show that the plethysmograms acquired with the new design are high in quality, clearly showing the morphological characteristics of the pulse waves that provide relevant information. Furthermore, tests performed with the new pulse oximeter estimated HR and SpO_2 values very similar to those provided by other commercial pulse oximeters.

II. New Proposal for a Pulse Oximeter Circuit

A. Design of the Pulse Oximeter

Fig. 3 shows the new circuit to obtain plethysmograms from the red and IR wavelengths generated by the two LEDs. As explained in the following, the circuit obtains these plethysmograms by performing a light-to-time-to-digital conversion. In addition to the LEDs, the photodiode, and the three pins of the DP shown in Fig. 3, the circuit uses only two resistors, R_{IR} and R_R, and one capacitor, C. The DP can be a microprocessor, part of an ASIC that includes the circuitry shown in Fig. 3, or even an FPGA if the device is designed for research purposes, as in this article. The DP will also be in charge of processing the digital data it generates in order to obtain the HR and SpO_2 values. The new circuit eliminates the need for TIAs, voltage amplifiers, voltage references, ADCs, or SIs, bringing savings in terms of both hardware and area. Capacitor C in Fig. 3 replaces all these elements in the circuits of Figs. 1 and 2 (note that R_R and R_{IR} resistors, connected to a voltage source, are also required on the pulse oximeters in Figs. 1 and 2).

For the DP pins, O_{IR} and O_R should be outputs that allow the LED activation time intervals to be selected. The pin that will establish the time measurements, P_C, must be able to be configured as input–output. If configured as an input, it should have a very high input impedance ("HZ-In" state).

TABLE I
Steps to Obtain Time Measurements for Red and IR Plethysmograms

STEPS	STATE OF PINS O_R	O_{IR}	P_C	MEASUREMENT
Ch. – Charging	'0'	'0'	'1'	
DR. – Discharging with Red LED ON, IR LED OFF	'1'	'0'	'HZ-In'	T_R
Ch. – Charging	'0'	'0'	'1'	
DIR. – Discharging with Red LED OFF, IR LED ON	'0'	'1'	'HZ-In'	T_{IR}

Each data point in a plethysmogram generated with the new circuit is a time measurement from a C discharge process. These measurements are expressed in a number of DP internal clock cycles. The steps to obtain these measurements are shown in Table I, indicating the logic state of the DP pins in each step. The four-step sequence shown in Table I, **Ch-DR-Ch-DIR**, is repeated to obtain a datum for each plethysmogram. Thus, the plethysmograms are obtained in an interleaved manner, with each measurement of the red plethysmogram being followed by one of the IR plethysmograms.

The LEDs are off during **Ch** due to the "0" output of O_R and O_{IR}, meaning virtually no current flows through the photodiode, and C charges up to the maximum voltage, V_{DD}, that the P_C pin can provide when configured as a "1" output. The length of **Ch** may vary when previously C is discharged by the IR LED, $T_{ch,R}$, or by the red LED, $T_{ch,IR}$. Varying the charging times allows the maintenance of a stable sampling frequency to obtain the data. In any case, these times must allow a stable voltage to be reached in C and, therefore, depend on the current provided by pins O_R and O_{IR}, the value of the resistances, R_{IR} and R_R, and the capacitance, C.

Once C is charged, the P_C pin changes to the "HZ-In" state, and one of the LEDs is activated (**DR** or **DIR** steps in Table I). The amount of light that the photodiode receives from the activated LED, either by transmission or by reflection through a finger or earlobe, increases the reverse current that circulates through it (I_{PD} in Fig. 3), varying the discharge rate of the capacitor. As the P_C pin has been set to the "HZ-In" state, it does not influence the C discharging process. The time measurements obtained during the **DR** or **DIR** steps (T_R or T_{IR}, respectively) are taken from the beginning of the discharging to the instant, in which the P_C pin detects a change of logic state in the V_C voltage of Fig. 3. This situation occurs for $V_C = V_{TL}$, where V_{TL} is the threshold voltage of the P_C pin for the transition from "1" to "0." The time evolutions of the voltages on the DP pins V_{IR}, V_R, and V_C are shown in Fig. 4.

On the other hand, obtaining a stable sampling period, T_S, requires the following (see Fig. 4):

$$T_{IR} + T_{ch,R} = T_R + T_{ch,IR} = \frac{T_S}{2}. \quad (1)$$

As stated, this implies that $T_{ch,R}$ and $T_{ch,IR}$ change after each measurement. In any case, the selected value of T_S must ensure

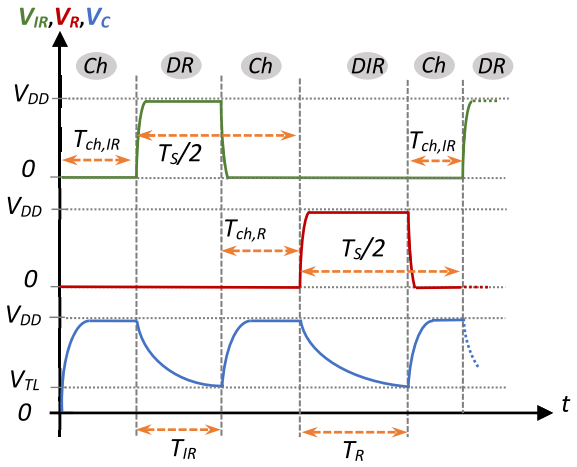

Fig. 4. Voltage waveforms for V_R, V_{IR}, and V_C in the circuit of Fig. 3 and for the different steps of Table I.

a minimum value for $T_{ch,R}$ and $T_{ch,IR}$ when the maximum values of T_{IR} and T_R are reached, which determines the maximum sampling frequency.

The value of a discharge time measurement when activating any of the LEDs, T_M, can be evaluated by analyzing the circuit formed by the capacitor and photodiode in Fig. 3. Let us consider that I_{PD} can be written as

$$I_{PD} = I_P - I_D \tag{2}$$

where I_P is the photocurrent due to the incident light on the photodiode, and I_D is the dark current given by

$$I_D = I_S\left(e^{-qV_C/k_BT} - 1\right) \tag{3}$$

where I_S is the reverse saturation current, q is the electron charge, k_B is the Boltzmann constant, and T is the absolute temperature. Since the evolution of $V_C(t)$ during capacitor discharge is due solely to I_{PD}, we can write

$$I_{PD} = -C\frac{dV_C}{dt}. \tag{4}$$

Substituting the value of I_{PD} given by (2) and (3) in this expression, the following differential equation is obtained:

$$dt = \frac{C \cdot dV_C}{I_S\left(e^{-qV_C/k_BT} - 1\right) - I_P}. \tag{5}$$

Finding T_M simply requires us to integrate the right-hand term of this expression between the capacitor's initial and final voltage during the discharge process (V_{DD} and V_{TL}, respectively)

$$T_M = \int_{V_{TL}}^{V_{DD}} \frac{C \cdot dV_C}{I_S\left(e^{-qV_C/k_BT} - 1\right) - I_P}. \tag{6}$$

The integral can be evaluated by performing the change of variable

$$x = I_S e^{-qV_C/k_BT}. \tag{7}$$

Such that, (6) becomes

$$T_M = \frac{Ck_BT}{q(I_S + I_P)} \cdot \int_{x_i}^{x_f} \left(\frac{1}{x} + \frac{1}{I_S + I_P - x}\right) \cdot dx \tag{8}$$

where $x_i = x(V_C = V_{DD})$ and $x_f = x(V_C = V_{TL})$.

If we assume that incident light power is constant during the short duration of the C discharge, then I_P is also constant, and from (8), we find

$$T_M = \frac{C}{I_S + I_P} \cdot \left[(V_{DD} - V_{TL}) + \frac{k_BT}{q} \times \ln\left(\frac{I_S\left(1 - e^{-qV_{DD}/k_BT}\right) + I_P}{I_S\left(1 - e^{-qV_{TL}/k_BT}\right) + I_P}\right)\right]. \tag{9}$$

This expression can be simplified by taking into account, first, that the natural logarithm in (9) approaches zero, since

$$\frac{k_BT}{q} \ll V_{DD}, \quad V_{TL} \tag{10}$$

and second, the term that multiplies the natural logarithm verifies

$$\frac{k_BT}{q} \ll V_{DD} - V_{TL}. \tag{11}$$

Such that the second term in square brackets is much smaller than the first, and (9) is just

$$T_M \approx C \cdot \frac{V_{DD} - V_{TL}}{I_S + I_P}. \tag{12}$$

It is important to note that (12) is obtained for a photodiode with a reverse bias voltage that varies during the discharge process. In contrast, reverse bias voltages are constant in the photodiodes of Figs. 1 and 2. T_M in (12) can also be expressed more conveniently, considering that I_P has a component due to ambient light, I_{AL}, and a component due to reflected/transmitted light, I_{RT}, such that

$$I_P = I_{AL} + I_{RT}. \tag{13}$$

Finally, (12) is

$$T_M \approx C \cdot \frac{V_{DD} - V_{TL}}{I_o + I_{RT}} \tag{14}$$

where $I_o = I_S + I_{AL}$ is a constant term during the discharging time and satisfies $I_o \ll I_{RT}$ (carefully selecting the photodiode and reducing ambient light). Thus, (14) reduces to

$$T_M \approx C \cdot \frac{V_{DD} - V_{TL}}{I_{RT}}. \tag{15}$$

This equation shows the inverse relationship between T_M and I_{RT}.

B. HR and SpO_2 Values

As shown in (15), the information provided by T_M is identical to that provided by I_{RT}. Next, it is demonstrated how, from the different T_M values, it is possible to obtain HR and SpO_2 similar to how it is carried out in a pulse oximeter based on the circuits in Figs. 1 and 2.

In the simplest cases, HR can be calculated from the difference between the times at which the minimum I_{IR} values occur in a cycle i and in a cycle $i + n$ of the plethysmogram (n is an integer selected by the designer to provide greater stability in the HR value). It should be noted that these instants match those in which the peaks of the plethysmogram formed from the measurements T_{IR} occur, as deduced from (15).

If $t_{IR}(\text{peak}_i)$ and $t_{IR}(\text{peak}_{i+n})$ are the times at which the ith and the $(i + \text{n})$th peaks in T_{IR} are reached, respectively, then, HR, in beats per minute (BPM), can be calculated as

$$\text{HR} = 60 \cdot n \cdot \frac{1}{t_{IR}(\text{peak}_{i+n}) - t_{IR}(\text{peak}_i)}. \tag{16}$$

There are other more complex methods for estimating HR that considers the existence of motion artifacts [31], [32], but this falls outside the scope of this article.

The ac and dc values of I_{RT} for the red and IR wavelengths are needed to find the SpO_2 values [33]. The dc value corresponds to the I_{RT} value for basal blood flow, i.e., the maximum value of I_{RT} in one pulse cycle. In comparison, the ac value is the difference between the maximum and minimum values of I_{RT} during one pulse cycle.

Let $I_{RT,R}(\text{trough})$ and $I_{RT,IR}(\text{trough})$ be the minimum values of I_{RT} in a cycle of the red and IR plethysmogram, respectively, with $I_{RT,R}(\text{peak})$ and $I_{RT,IR}(\text{peak})$ being their maximum values. The ac and dc values of I_{RT} in a cycle of the red and IR plethysmograms $I_{RT,R}(\text{ac})$, $I_{RT,R}(\text{dc})$, $I_{RT,IR}(\text{ac})$, and $I_{RT,IR}(\text{dc})$ are, therefore, given by

$$I_{RT,R}(\text{ac}) = I_{RT,R}(\text{peak}) - I_{RT,R}(\text{trough}) \tag{17}$$

$$I_{RT,R}(\text{dc}) = I_{RT,R}(\text{peak}) \tag{18}$$

$$I_{RT,IR}(\text{ac}) = I_{RT,IR}(\text{peak}) - I_{RT,IR}(\text{trough}) \tag{19}$$

$$I_{RT,IR}(\text{dc}) = I_{RT,IR}(\text{peak}). \tag{20}$$

Meanwhile, the perfusion ratios, P_R and P_{IR}, are required to find the SpO_2 value

$$P_R = \frac{I_{RT,R}(\text{ac})}{I_{RT,R}(\text{dc})} \tag{21}$$

$$P_{IR} = \frac{I_{RT,IR}(\text{ac})}{I_{RT,IR}(\text{dc})}. \tag{22}$$

With these definitions, the normalized absorption ratio, R, is defined as

$$R = \frac{P_R}{P_{IR}} = \frac{I_{RT,R}(\text{ac})/I_{RT,R}(\text{dc})}{I_{RT,IR}(\text{ac})/I_{RT,IR}(\text{dc})}. \tag{23}$$

However, the new circuit provides plethysmograms based on time rather than current measurements. Obtaining R as a function of time measurements requires the following values derived from (15):

$$T_R(\text{peak}) = \frac{C(V_{DD} - V_{TL})}{I_{RT,R}(\text{trough})} \tag{24}$$

$$T_R(\text{trough}) = \frac{C(V_{DD} - V_{TL})}{I_{RT,R}(\text{peak})} \tag{25}$$

$$T_{IR}(\text{peak}) = \frac{C(V_{DD} - V_{TL})}{I_{RT,IR}(\text{trough})} \tag{26}$$

$$T_{IR}(\text{trough}) = \frac{C(V_{DD} - V_{TL})}{I_{RT,IR}.(\text{peak})}. \tag{27}$$

Meaning (21) and (22) can be written

$$P_R = \frac{T_R(\text{peak}) - T_R(\text{trough})}{T_R(\text{peak})} \tag{28}$$

$$P_{IR} = \frac{T_{IR}(\text{peak}) - T_{IR}(\text{trough})}{T_{IR}(\text{peak})} \tag{29}$$

and, with these values, (23) is

$$R = \frac{T_{IR}(\text{peak})}{T_R(\text{peak})} \cdot \frac{T_R(\text{peak}) - T_R(\text{trough})}{T_{IR}(\text{peak}) - T_{IR}(\text{trough})}. \tag{30}$$

Finally, from R, it is found in [34] that

$$SpO_2 = \frac{0.81 - 0.18 \cdot R}{0.63 + 0.11 \cdot R} \times 100\%. \tag{31}$$

In practice, however, SpO_2 is assumed to be a linear function of R

$$SpO_2 = a - b \cdot R \tag{32}$$

where a and b are constants obtained by calibration.

With the new circuit, the SpO_2 value is therefore ascertained from the plethysmogram maximums and minimums during a pulse wave using (30) and linear equation (32). This procedure is very common for obtaining SpO_2, although other more complex methods relate R to SpO_2 [35].

C. Errors and Uncertainties

The main source of error when using (15) to form the plethysmograms is the photodiode capacitor C_{PD}, which in the circuit in Fig. 3 is located in parallel with C. Considering this capacitor C should be replaced by $C_{PD} + C$ in (4). If C_{PD} is a constant, this element would not be a problem for determining R or SpO_2 since (30) does not show any dependence on the capacitance of the circuit. However, C_{PD} varies slightly with the voltage applied to the photodiode and cannot be handled as a constant in (6). Fortunately, C_{PD} is in the range of just a few picofarads, and its variations, C_{PD}, maybe even smaller. It is, therefore, possible to choose C in such a way that $C \gg C_{PD}$, while simultaneously keeping T_R and T_{IR} small enough to consider a constant value of I_{PD} during discharge.

Meanwhile, the presence of C_{PD} does not modify the HR value since it does not vary the instants of time, in which the peaks and troughs are reached in the plethysmograms.

On the other hand, errors in the precise determination of R_R and R_{IR} have no practical importance since their only effect is a slight modification of $I_{RT,R}$ and $I_{RT,IR}$ and, therefore, of the temporal measurements. However, the modification occurs in the same way in all these measurements, as indicated by (15), and consequently, it does not affect the HR and SpO_2 calculations. For the same reason, it is not necessary to consider the output resistors of the FPGA pins since their values are generally low.

Since R and SpO_2 depend on time measurements, the uncertainty in their estimates, $u(R)$ and $u(SpO_2)$, comes from the uncertainty in their time measurements, $u(T_M)$. There are two causes for $u(T_M)$ [36]. The first one is quantization in clock cycles of the time measurements, which produces quantization uncertainty. However, this uncertainty can be neglected if the values of T_M (expressed in DP clock cycles) are large enough. Thus, the most important cause of uncertainty is the electronic noise in V_C at the trigger instant. This uncertainty, u_{trigger}, depends inversely on the slope of the discharge curve of V_C when it reaches voltage V_{TL} [37]

$$u_{\text{trigger}} = \frac{\alpha}{\left| dV_C(t)/dt \right|_{V_C = V_{TL}}} \tag{33}$$

being α, a constant related to the noise level in the circuit's node. Meanwhile, whenever the same conditions that led to (15) are verified, it is trivial to obtain from (4)

$$V_C(t) = V_{DD} - \frac{I_{RT} \cdot t}{C} \tag{34}$$

and (33) becomes

$$u(T_M) \approx u_{\text{trigger}}(T_M) = \frac{\alpha \cdot C}{I_{RT}}. \tag{35}$$

This expression allows us to find a quality measurement in the estimation of T_M, $u(T_M)/T_M$ using (14)

$$\frac{u(T_M)}{T_M} = \frac{\alpha}{V_{DD} - V_{TL}}. \tag{36}$$

Thus, $u(T_M)/T_M$ is constant, regardless of C, for a given noise level in the circuit. It, therefore, makes no sense to increase C, to achieve higher quality in T_M, beyond a value that allows us to neglect quantization uncertainty and which verifies $C \gg C_{PD}$.

On the other hand, to find the quality in the estimation of R, $u(R)/R$, it must be remembered that R in (30) is a function of four measurements: T_R(peak), T_R(trough), T_{IR}(peak), and T_{IR}(trough). Since T_M can be any of these time measurements, we can write

$$\frac{u(R)}{R} = \frac{1}{R}\sqrt{\sum_{T_M}\left(\frac{\partial R}{\partial T_M}\right)^2 u^2(T_M)}. \tag{37}$$

Using (28)–(30) and (36), after some simple algebraic operations, (37) becomes

$$\frac{u(R)}{R} = \frac{2\alpha}{V_{DD} - V_{TL}}\sqrt{\left[\left(\frac{1}{P_R} - 1\right)^2 + \left(\frac{1}{P_{IR}} - 1\right)^2\right]}. \tag{38}$$

Thus, quality in estimating R depends on physiological parameters, P_R and P_{IR} (which the designer has no influence over), and electrical noise in V_C, which the designer must try to minimize. Nevertheless, P_R and P_{IR} are much less than one and (38) can be approximated by a constant value

$$\frac{u(R)}{R} = \frac{\sqrt{8} \cdot \alpha}{V_{DD} - V_{TL}}. \tag{39}$$

Finally, using (32), quality in estimating SpO_2 is given by

$$\begin{aligned}\frac{u(SpO_2)}{SpO_2} &= \left|\frac{d\,SpO_2}{dR}\right|\frac{u(R)}{SpO_2} = \frac{b}{SpO_2}u(R) \\ &= \left(\frac{a}{SpO_2} - 1\right) \cdot \frac{u(R)}{R}.\end{aligned} \tag{40}$$

This result shows that quality in estimating SpO_2 depends on quality in estimating R and on the SpO_2 value itself. This phenomenon also occurs in pulse oximeters based on the circuits in Figs. 1 and 2. However, for usual values of a and SpO_2

$$\frac{a}{SpO_2} - 1 \ll 1 \tag{41}$$

and

$$\frac{u(SpO_2)}{SpO_2} \ll \frac{u(R)}{R}. \tag{42}$$

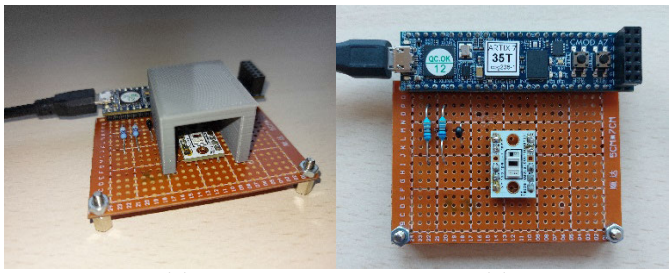

(a) (b)

Fig. 5. Implemented circuit. (a) With a cavity for finger insertion and (b) without the cover on the SFH7072.

III. Methods, Experimental Results, and Discussion

As a proof of concept of the new pulse oximeter, the circuit has been designed using a commercial board, namely, the Digilent CMOD A7 (Pullman, Washington). This board uses an FPGA (Xilinx Artix 7 XC7A35T) that will perform the DP functions in the pulse oximeter, with 3.3 V as the V_{DD} value for the pins. Using an FPGA has the advantage of allowing rapid prototyping of the circuit in Fig. 3, while also helping to assess the complexity of a future ASIC that includes the entire circuit. The characteristics of the pins (configured as output pins) of this FPGA ensure (together with resistors R_R and R_{IR}) the current required for ON/OFF control of the LEDs. When configured as an input, a pin presents a very high input impedance, as occurs with the P_C pin in Fig. 3. In the board, the FPGA is connected to a UART port interface integrated circuit, FT2232HQ. This port connects the circuit to a laptop to transmit the T_R and T_{IR} data obtained by the FPGA and the HR and SpO_2 values. It is, therefore, possible to check the accuracy of the estimates, comparing those made internally in the FPGA with those found using the MATLAB software. The FPGA's internal clock frequency is set at 100 MHz. The time measurements count is therefore incremented every 10 ns. The threshold voltage, V_{TL}, measured experimentally in the P_C pin is approximately 1.26 V (this is the minimum value of the reverse bias voltage of the photodiode when obtaining T_M).

The red and IR LEDs and the photodiode in the circuit of Fig. 3 are in a single device, the SFH7072 by OSRAM (Berkshire, U.K.). A value of 350 Ω has been selected for R_R and R_{IR}, limiting the turn-on current of the LEDs to approximately 4 mA (choosing the optimal values of resistors R_R and R_{IR} shall be a topic to return to in future works). A capacitance of 1 nF has been selected considering all set out above on the value of C. All these elements have been connected to the CMOD A7 on a solderable breadboard for rapid prototyping. Fig. 5 shows the implemented system.

The internal structure programmed into the FPGA is shown in Fig. 6. It displays a 16-bit ring counter with an end of count (EOC) output to indicate the start of a discharging process to the control unit. The count is incremented whenever a "1" is detected during discharging or in the **Ch** steps. The values generated by the counter, T_R and T_{IR}, are taken directly to the control unit and the arithmetic unit. The operations

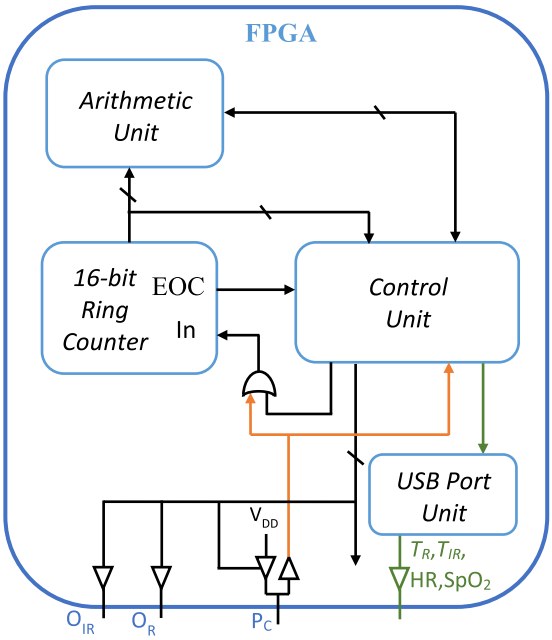

Fig. 6. Internal structure programmed in the FPGA.

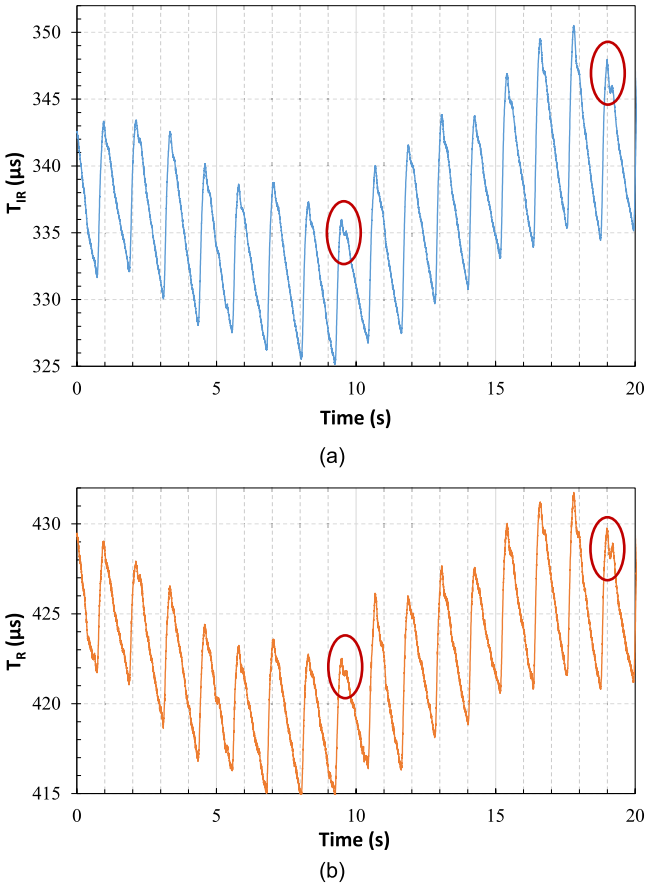

Fig. 7. Plethysmograms obtained during a time interval of 20 s with the new proposed circuit. (a) For the IR wavelength, with T_{IR} measurements in μs. (b) For the red wavelength, with T_R measurements in μs.

in the arithmetic unit are simple since only the search for the maximums and minimums of T_R and T_{IR} is carried out, using these values together with (16), (30), and (32) to obtain HR and SpO_2. Finally, all these data are input into the USB port unit, which communicates with the FT2232HQ for data transmission to the laptop.

The T_R and T_{IR} values, as received in the laptop, allow us to obtain plethysmograms, such as the two shown in Fig. 7. In these plethysmograms, the vertical axis shows the T_R and T_{IR} values in microseconds; however, as mentioned, the FPGA obtains the values in number of clock cycles. The count varies between 32 500 and 35 000 for the IR plethysmogram, while the variation for the red plethysmogram is between 41 500 and 43 500. The 16-bit ring counter provides these values in Fig. 6, whose maximum count value, $2^{16} - 1 = 65\,535$, has proven to be sufficient in all tests performed.

As discussed in Section II, (1) must be verified to maintain a constant sampling period. To do this and ensure full charge of C, the FPGA state changes to **Ch** once T_R or T_{IR} is detected and continues in this state until the counter (which has not been stopped) reaches its maximum value. At this point, the process of obtaining a measurement on the other plethysmogram begins. Thus, the minimum duration of the **Ch** step is $65\,535 - 43\,500 = 22\,035$ clock cycles.

Proceeding in this way, $T_S = 2{\cdot}65535{\cdot}10$ ns. That is, the sampling frequency with which each plethysmogram is obtained is 763 Hz.

It is worth mentioning that the proposed circuit allows the adoption of sampling techniques that reduce the number of samples to generate the characteristic points of a plethysmogram, such as compressive sampling or event-driven sampling [25]. It is enough to modify the control unit in Fig. 6 to use these techniques, introducing variable periods of time with the LEDs off.

The two plethysmograms in Fig. 7 show how, with this sampling frequency, the details of the pulse wave can be observed quite accurately, in addition to the slow evolution of the basal level. Meanwhile, Fig. 7(b) also shows a slightly higher signal noise level for the red wavelength than for the IR wavelength of Fig. 7(a), as is typical of all pulse oximeters. The perfusion ratios obtained from these plethysmograms, P_R and P_{IR}, present normal values, around 2% and 3%, respectively [note that these values make the approximation (39) possible].

The different pulse waves and their identifying characteristics can be observed in time and amplitude. Hence, in Fig. 7, it is easy to distinguish the appearance of two dicrotic pulses [38], highlighted in red. The dicrotic pulse located furthest to the right has been amplified in Fig. 8, for the IR wavelength, clearly showing the resolution obtained in determining its characteristics. Pulse waves are characterized by their systolic amplitude, diastolic amplitude, and dicrotic notch; all these parameters are shown in Fig. 8.

It is important to note that Figs. 7 and 8 show the raw data obtained by the FPGA without any type of digital processing (such as filtering). Obtaining this information allows us to establish physiological parameters of clinical interest, e.g., augmentation, crest time, large artery stiffness index (LASI), or inflection point area ratio (IPA) [39].

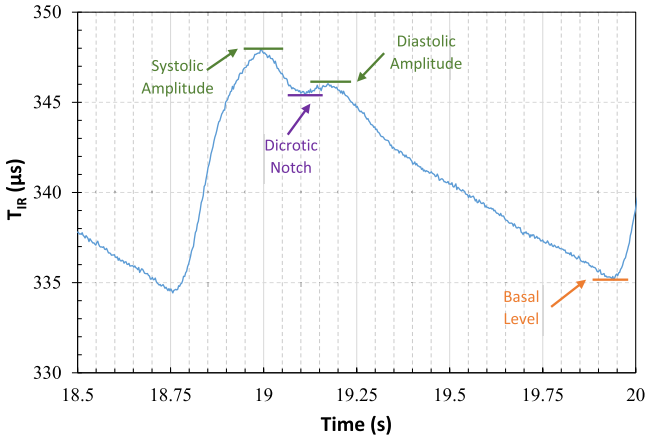

Fig. 8. Magnification of the second dicrotic pulse marked in red in Fig. 7(a), where the most important features of the dicrotic pulse wave in the IR plethysmogram are presented in more detail.

TABLE II
COMPARISON

Subject	Pulse Oximeter SpO_2 / HR (MAE) [% / BPM (BPM)]		
	1	2	This work
#1	96 / 54 (1.2)	97 / 55 (0.2)	96.3 / 55.9 (0.7)
#2	96 / 58 (0.8)	98 / 59 (0.2)	95.1 / 59.1 (0.3)
#3	98 / 73 (0.9)	99 / 74 (0.1)	97.3 / 74.1 (0.2)
#4	96 / 54 (1.8)	98 / 53 (0.8)	95.5 / 51.6 (0.6)
#5	96 / 46 (2.2)	99 / 47 (1.2)	94.8 / 48.1 (0.1)
#6	96 / 60 (0.8)	99 / 58 (2.8)	97.0 / 61.2 (0.4)
#7	96 / 88 (1.2)	99 / 88 (1.2)	98.0 / 89.0 (0.2)
#8	95 / 82 (1.3)	97 / 83 (0.3)	94.6 / 83.3 (0)

For the HR and SpO_2 values obtained by the new pulse oximeter:

1) Value $n = 10$ was chosen to estimate HR using (16). Thus, each pulse wave generates a new HR value considering the last ten pulse waves for calculation.
2) Obtaining the SpO_2 value using (32) requires us to know a and b in this equation. The commonly used empirical values for these parameters are [29] $a = 110$ and $b = 25$.

For a simple and functional comparison, eight apparently healthy subjects (for whom informed consent was obtained) were selected to estimate HR and SpO_2 values. The tests were performed in a fixed state without any movement. The estimates were obtained using the new circuit and two commercial pulse oximeters. The first of the commercial pulse oximeters, labeled Pulse Oximeter 1 in Table II, is the Vitalcontrol model by Hans Dinslage GmbH (Uttenweiler, Germany) with ±2% accuracy for SpO_2 ranging from 70% to 100% and ±2 beats/minute for HR ranging from 30 to 250. The second, labeled Pulse Oximeter 2, is the FarmaqO from Farmaqo (Fresnes, France) with ±2% accuracy for SpO_2 ranging from 70% to 100% and ±3 beats/minute for HR ranging from 25 to 250. The results are shown in Table II, where the HR values are expressed in BPM, and the SpO_2 values are expressed as a percentage. The results were taken simultaneously for the three pulse oximeters placed on different fingers for 20 s. For commercial pulse oximeters, the values in Table II are those that were most prolonged during the 20 s, while for the new circuit, they are the average values during this time.

Table II shows an acceptable agreement between the values of the three pulse oximeters. The SpO_2 values estimated by the new circuit are generally closer to those of Pulse Oximeter 1, while the HR values are closer to those of Pulse Oximeter 2. Table II also shows the mean absolute errors (MAEs) of the HR estimates obtained from the manual examination of the data recorded with the experimental setup shown in Fig. 5.

IV. Conclusion

Current implementations of pulse oximeters require complex circuits to acquire and digitalize the pulse wave signal. Apart from the photodiodes and LEDs required to obtain the plethysmograms used by pulse oximeters, these circuits need a variable number of analog modules, together with an ADC or an SI. Furthermore, all implementations require a DP, which, operating on the acquired data, provides at least the HR and SpO_2 values.

This article presents a new circuit for a pulse oximeter that eliminates the need for such analog modules, ADCs, and SIs. Logically, the circuit needs the same photodiodes and LEDs as other implementations but uses only two resistors to control the LEDs, a capacitor, and the DP. The circuit reduces the hardware required by means of a light-to-time-to-digital conversion, which takes advantage of the characteristics of the pins of the DPs. The new proposal does not impose any special restrictions on the DP used in the circuit, giving the designer the freedom to select microcontrollers, FPGAs, or ASICs as the pulse oximeter's digital core.

As proof of concept, the circuit has been implemented using an FPGA as the DP. The results show plethysmograms with resolution levels (both in amplitude and time) that allow the characteristics of the pulse waves to be clearly distinguished, allowing the pulse oximeter to be used for clinical purposes.

A simple comparison of the new design's performance with two commercial pulse oximeters has found no significant differences between the HR or SpO_2 values provided by the commercial pulse oximeters and those estimated with the new circuit.

Acknowledgment

The author would like to thank Prof. Manuel J. Martín-Vázquez and Prof. José F. Martín-Canales for their selfless help.

References

[1] E. Gil, M. Orini, R. Bailón, J. M. Vergara, L. Mainardi, and P. Laguna, "Photoplethysmography pulse rate variability as a surrogate measurement of heart rate variability during non-stationary conditions," *Physiolog. Meas.*, vol. 31, no. 9, pp. 1271–1290, Sep. 2010.

[2] N. Netzer, A. H. Eliasson, C. Netzer, and D. A. Kristo, "Overnight pulse oximetry for sleep-disordered breathing in adults," *Chest*, vol. 120, no. 2, pp. 625–633, Aug. 2001.

[3] A. J. Enoch, M. English, and S. Shepperd, "Does pulse oximeter use impact health outcomes? A systematic review," *Arch. Disease Childhood*, vol. 101, no. 8, pp. 694–700, Aug. 2016.

[4] S. Karolcik, D. K. Ming, S. Yacoub, A. H. Holmes, and P. Georgiou, "A multi-site, multi-wavelength PPG platform for continuous non-invasive health monitoring in hospital settings," *IEEE Trans. Biomed. Circuits Syst.*, vol. 17, no. 2, pp. 349–361, Apr. 2023.

[5] S. Akdemir Akar, S. Kara, F. Latifoğlu, and V. Bilgiç, "Spectral analysis of photoplethysmographic signals: The importance of preprocessing," *Biomed. Signal Process. Control*, vol. 8, no. 1, pp. 16–22, Jan. 2013.

[6] J. E. Sinex, "Pulse oximetry: Principles and limitations," *Amer. J. Emergency Med.*, vol. 17, no. 1, pp. 59–66, Jan. 1999.

[7] X. Geng, Y. Zhang, J. Zhang, Y. Wang, and H. Zhang, "Time-domain feature parameter extraction algorithm of pulse wave based on morphological features," *Front. Artif. Intell. Appl.*, vol. 363, pp. 555–566, 2022.

[8] Z. Lu, X. Chen, Z. Dong, Z. Zhao, and X. Zhang, "A prototype of reflection pulse oximeter designed for mobile healthcare," *IEEE J. Biomed. Health Informat.*, vol. 20, no. 5, pp. 1309–1320, Sep. 2016.

[9] S. Kumar, "A review of transimpedance amplifiers used in biomedical applications," in *Proc. 5th Int. Conf. Comput. Methodolog. Commun. (ICCMC)*, Athens, Greece, Apr. 2021, pp. 1314–1321.

[10] E. F. Pribadi, R. K. Pandey, and P. C.-P. Chao, "Design and implementation of a new light to digital converter for the PPG sensor," *Microsyst. Technol.*, vol. 27, no. 6, pp. 2461–2472, Jun. 2021.

[11] M. Tavakoli, L. Turicchia, and R. Sarpeshkar, "An ultra-low-power pulse oximeter implemented with an energy-efficient transimpedance amplifier," *IEEE Trans. Biomed. Circuits Syst.*, vol. 4, no. 1, pp. 27–38, Feb. 2010.

[12] M. Alhawari, N. A. Albelooshi, and M. H. Perrott, "A 0.5 V $< 4\mu$W CMOS light-to-digital converter based on a nonuniform quantizer for a photoplethysmographic heart-rate sensor," *IEEE J. Solid-State Circuits*, vol. 49, no. 1, pp. 271–288, Jan. 2014.

[13] E. M. G. Rodrigues, R. Godina, C. M. P. Cabrita, and J. P. S. Catalão, "Experimental low cost reflective type oximeter for wearable health systems," *Biomed. Signal Process. Control*, vol. 31, pp. 419–433, Jan. 2017.

[14] B. Lin, Z. Ma, M. Atef, L. Ying, and G. Wang, "Low-power high-sensitivity photoplethysmography sensor for wearable health monitoring system," *IEEE Sensors J.*, vol. 21, no. 14, pp. 16141–16151, Jul. 2021.

[15] G. Di, X. Tang, and W. Liu, "A reflectance pulse oximeter design using the MSP430F149," in *Proc. IEEE/ICME Int. Conf. Complex Med. Eng.*, Beijing, China, May 2007, pp. 1081–1084.

[16] A. K. Reddy, G. Boby, M. N. Mohan, and J. V. Kumar, "A novel method for the measurement of oxygen saturation in arterial blood," in *Proc. IEEE Int. Instrum. Meas. Technol. Conf.*, May 2011, pp. 1–5.

[17] K. Li and S. Warren, "A wireless reflectance pulse oximeter with digital baseline control for unfiltered photoplethysmograms," *IEEE Trans. Biomed. Circuits Syst.*, vol. 6, no. 3, pp. 269–278, Jun. 2012.

[18] J. Graeme, *Photodiode Amplifiers: Op Amp Solutions*. New York, USA: McGraw-Hill, 1995.

[19] J. Rhee, J. Park, and S. Kim, "A 0.3 lx–1.4 mlx monolithic silicon nanowire light-to-digital converter with temperature-independent offset cancellation," *IEEE J. Solid-State Circuits*, vol. 55, no. 2, pp. 378–391, Feb. 2020.

[20] K. N. Glaros and E. M. Drakakis, "A sub-mW fully-integrated pulse oximeter front-end," *IEEE Trans. Biomed. Circuits Syst.*, vol. 7, no. 3, pp. 363–375, Jun. 2013.

[21] S. V. Gubbi and B. Amrutur, "Adaptive pulse width control and sampling for low power pulse oximetry," *IEEE Trans. Biomed. Circuits Syst.*, vol. 9, no. 2, pp. 272–283, Apr. 2015.

[22] F. Tang et al., "A low power and fast tracking light-to-frequency converter with adaptive power scaling for blood SpO_2 sensing," *IEEE Trans. Biomed. Circuits Syst.*, vol. 13, no. 1, pp. 26–37, Feb. 2019.

[23] F. Tang et al., "A noise-reduced light-to-frequency converter for sub-0.1% perfusion index blood SpO_2 sensing," *IEEE Trans. Biomed. Circuits Syst.*, vol. 14, no. 5, pp. 931–941, Oct. 2020.

[24] G. Di Patrizio Stanchieri, A. De Marcellis, M. Faccio, E. Palange, and U. Guler, "A new light-to-frequency analog front-end circuit for optical sensing in biomedical applications," in *Proc. IEEE Biomed. Circuits Syst. Conf. (BioCAS)*, Berlin, Germany, Oct. 2021, pp. 1–5.

[25] Z. Ebrahimi and B. Gosselin, "Ultralow-power photoplethysmography (PPG) sensors: A methodological review," *IEEE Sensors J.*, vol. 23, no. 15, pp. 16467–16480, Aug. 2023.

[26] F. Reverter, F. Vidal-Verdú, and J. A. Hidalgo-Lopez, "Advanced techniques for directly interfacing resistive sensors to digital systems," in *Smart Sensors, Measurement and Instrumentation*, vol. 25. Cham, Switzerland: Springer, 2017, pp. 139–165.

[27] J. A. Hidalgo-López and J. Castellanos-Ramos, "Two proposals to simplify resistive sensor readout based on resistance-to-time-to-digital conversion," *Measurement*, vol. 213, May 2023, Art. no. 112728.

[28] J. A. Hidalgo-López and J. Castellanos-Ramos, "Simplifying capacitive sensor readout using a new direct interface circuit," *IEEE Trans. Instrum. Meas.*, vol. 72, pp. 1–10, 2023.

[29] Z. Kokolanski, F. Reverter, C. Gavrovski, and V. Dimcev, "Improving the resolution in direct inductive sensor-to-microcontroller interface," *Annu. J. Electron.*, vol. 9, pp. 135–138, Sep. 2015.

[30] Z. Czaja, "A microcontroller system for measurement of three independent components in impedance sensors using a single square pulse," *Sens. Actuators A, Phys.*, vol. 173, no. 1, pp. 284–292, Jan. 2012.

[31] A. Kr and B. M, "Heart rate estimation from photoplethysmography signal for wearable health monitoring devices," *Biomed. Signal Process. Control*, vol. 50, pp. 1–9, Apr. 2019.

[32] C. Wan, D. Chen, and J. Yang, "Pulse rate estimation from forehead photoplethysmograph signal using RLS adaptive filtering with dynamical reference signal," *Biomed. Signal Process. Control*, vol. 71, Jan. 2022, Art. no. 103189.

[33] M. W. Wukitsch, M. T. Petterson, D. R. Tobler, and J. A. Pologe, "Pulse oximetry: Analysis of theory, technology, and practice," *J. Clin. Monitor.*, vol. 4, no. 4, pp. 290–301, Oct. 1988.

[34] J. Webster, *Design Pulse Oximeters*. Boca Raton, FL, USA: CRC Press, 2002.

[35] P. Kainan, A. Sinchai, P. Tuwanut, and P. Wardkein, "New pulse oximetry detection based on the light absorbance ratio as determined from amplitude modulation indexes in the time and frequency domains," *Biomed. Signal Process. Control*, vol. 75, May 2022, Art. no. 103627.

[36] F. Reverter, J. Jordana, M. Gasulla, and R. Pallàs-Areny, "Accuracy and resolution of direct resistive sensor-to-microcontroller interfaces," *Sens. Actuators A, Phys.*, vol. 121, no. 1, pp. 78–87, May 2005.

[37] J. A. Hidalgo-López, Ó. Oballe-Peinado, J. Castellanos-Ramos, and J. A. Sánchez-Durán, "Two-capacitor direct interface circuit for resistive sensor measurements," *Sensors*, vol. 21, no. 4, p. 1524, Feb. 2021.

[38] O. Singh and R. K. Sunkaria, "Detection of onset, systolic peak and dicrotic notch in arterial blood pressure pulses," *Meas. Control*, vol. 50, nos. 7–8, pp. 170–176, Sep. 2017.

[39] F. Heydari, M. P. Ebrahim, J. M. Redoute, and M. R. Yuce, "Pulse wave characteristics based on age and body mass index (BMI) during sitting posture," in *Proc. BODYNETS*, Florence, Italy, 2019, pp. 125–132.